Accepted Manuscript

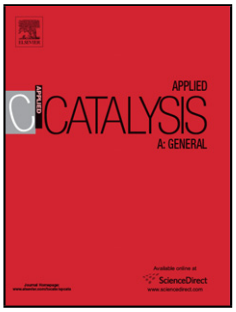

Title: Green synthesis of cavity-containing manganese oxides
with superior catalytic performance in toluene oxidation

Authors: Tomás García, José Manuel López, Álvaro Mayoral,
Yaping Zhang, Raul Arenal, Daniel Alonso-Domínguez,
María Pilar Pico, María Luisa López, Ana Dejoz, Inmaculada
Álvarez-Serrano, Rut Sanchis, Benjamín Solsona

PII: S0926-860X(19)30259-5
DOI: https://doi.org/10.1016/j.apcata.2019.06.005
Reference: APCATA 17107

To appear in: *Applied Catalysis A: General*

Received date: 13 February 2019
Revised date: 5 June 2019
Accepted date: 8 June 2019

Please cite this article as: García T, López JM, Mayoral Á, Zhang Y, Arenal R, Alonso-Domínguez D, Pico MP, López ML, Dejoz A, Álvarez-Serrano I, Sanchis R, Solsona B, Green synthesis of cavity-containing manganese oxides with superior catalytic performance in toluene oxidation, *Applied Catalysis A, General* (2019), https://doi.org/10.1016/j.apcata.2019.06.005

Green synthesis of cavity-containing manganese oxides with superior catalytic performance in toluene oxidation

Tomás García *[1,a], José Manuel López [a], Álvaro Mayoral [b], Yaping Zhang[b], Raul Arenal [c,d], Daniel Alonso-Domínguez [e], María Pilar Pico [f], María Luisa López [e], Ana Dejoz [g], Inmaculada Álvarez-Serrano *[2,e], Rut Sanchis [g], Benjamín Solsona*[3,g]

a. Instituto de Carboquímica (ICB-CSIC), C/Miguel Luesma 4, 50018 Zaragoza, Spain;.
b. Centre for High-Resolution Electron Microscopy (ChEM), School of Physical Science and Technology, ShanghaiTech University, 393 Middle Huaxia Road, Pudong, Shanghai, 201210, China.
c. Laboratorio de Microscopías Avanzadas, Instituto de Nanociencia de Aragón, Universidad de Zaragoza, 50018 Zaragoza, Spain
d. ARAID Foundation, 50018 Zaragoza, Spain.
e. Departamento de Química Inorgánica, Facultad de Ciencias Químicas, Universidad Complutense de Madrid; 28040 Madrid, Spain;+
f. Sepiolsa, Avda. del Acero, 14-16, Pol. UP-1 (Miralcampo), 19200 Azuqueca de Henares, Spain.
g. Departament d'Enginyeria Química, ETSE, Universitat de València, Av. Universitat, 46100 Burjassot, Valencia, Spain.

** Corresponding Authors: *1 tomas@icb.csic.es , *2 ias@ucm.es , *3 benjamín.solsona@uv.es*

Graphical abstract

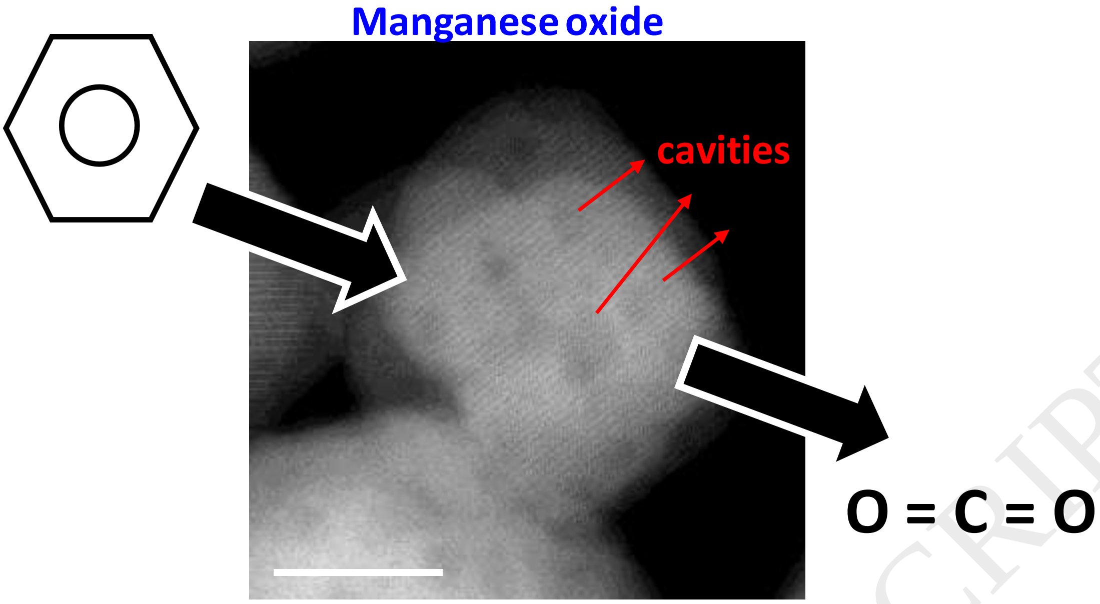

Highlights

- Green synthesis of cavity-containing manganese oxides by hydrothermal method
- High catalytic performance in toluene oxidation with total conversion at < 200ºC
- Highly reactive oxygen surface species at the tetragonal distorted cationic sites
- Presence of structural water and internal cavities in the Mn_3O_4 crystalline structure

Abstract

Manganese oxide prepared by a simple hydrothermal method is highly active and stable in both lab and quasi industrial conditions for the total oxidation of toluene, achieving total conversion at only 175ºC in the absence of water and at 150 °C in the presence of 4 mol % water. Moreover, this performance is stable for at least 6 cycles. The enhanced catalytic performance has been related to the presence of highly reactive oxygen surface species. This species are probably promoted by Mn_3O_4 nanoparticles with Mn^{3+} at the tetragonal distorted cationic sites, likely compensated by structural water at the anionic sites. The presence of structural water can be related to the formation of internal cavities/vesicles in the Mn_3O_4 crystalline structure.

Keywords: manganese oxide; cavities; structural water; toluene; VOCs oxidation.

1. Introduction

In the last decades, oxides of non-noble transition metals have been extensively investigated as catalysts for the total oxidation of volatile organic compounds (VOCs), due to the high price of the conventional catalysts which are based on noble metals (NM) [1,2]. Moreover, these NM-based catalysts permit to operate at temperatures ranging between 100 and 200 ºC. Among the non-NM oxides based catalysts; we can highlight pure and supported metal oxides of cobalt, copper, manganese or iron [3-8]. Manganese oxide catalysts have demonstrated to be highly active in the total oxidation of one-ring aromatics [9-11] and other subsets of VOCs [12-15].

Different synthetic routes, e.g. solid state, hydrothermal, molecular sieve techniques, lead to manganese oxide-based catalysts with high stability and great catalytic performance in the oxidation of aromatic compounds [16,17], e.g. a solvothermal technique combined with a calcination at 500ºC, reported as the most adequate for obtaining Mn(III) oxides-based catalysts [18]; and hydrolysis driven redox reactions leading to manganese oxide catalysts highly tolerant to moisture [19,20].

Hence, hydrothermal processes both in continuous and batch regimes have been employed for synthesizing inorganic particles in a wide variety of research fields, from functional ceramics and electronics to catalysis, biomass processing and energy storage devices [21-23]. Taking into account simplicity, low-cost and controllability criteria, solution-based processes stand out other synthetic strategies as they present saving energy benefits together with innocuous manipulation and tiptop control over particle size and morphology [24]. Hydrothermal routes are based on the chemical reactions and solubility changes of substances in a sealed heated aqueous solution above ambient temperature and pressure to grow nanocrystals [25]. Hence, in recent literature these environmentally benign hydrothermal techniques have been successfully employed for obtaining a great variety of materials with enhanced response for different specific fields; i.e. photocatalytic properties of MoS_2 [26], pseudocapacitive properties of NiS [27], photoelectrochemical performance of Sn-doped iron oxides [28], catalytic activity of $(Ti/Sn)O_2$ [29], electrochemical efficiency of organometal halide perovskites [30], supercapacitor response of hybrid electrodes [31], etc. In particular, manganese oxides with improved catalytic and electrochemical response [32] or enhanced adsorption performance [33] could be obtained by hydrothermal routes. Besides, solvothermal processes also permit to obtain nanoparticles with different morphologies and tuneable nanoarchitectures of functional materials [34].

Thus, it would be highly interesting to synthesize manganese oxides in a simple, sustainable and straightforward way maintaining the high reactivity and excellent stability. In this sense, hydrothermal synthesis, involving water as the only solvent, is revealed as one of the most simple, promising and green ways to prepare catalytically active materials [35]. Among the different manganese oxide crystalline phases, Kim et al. [14] reported that Mn_3O_4 is the most active phase in the total oxidation of benzene and toluene, which was associated to the best redox properties and the highest oxygen mobility. Later, other authors pointed out the high efficiency of γ-MnO_2 catalyst [11], interpreted on the basis of its three-dimensional macroporous and mesoporous morphology. In fact, VOC oxidation over these catalysts usually occurs through a Mars and van Krevelen (MVK) mechanism [36], where the hydrocarbon molecule is oxidised by lattice oxygen from the manganese oxide. The lattice oxygen is then replenished by the reduction of gaseous oxygen. Therefore, the availability and reactivity of surface oxygen species affect the activity of manganese oxides to a great extent, being the key parameter to develop high performance catalysts [37].

Herein, we report that a cavity-containing manganese oxide catalyst obtained by facile, low-cost and environmentally friendly hydrothermal (HT) process shows an outstanding catalytic activity in the removal of toluene by total oxidation. It is worth underlining the interest of the green synthetic route chosen, i.e. a hydrothermal process in which all the reactions take place in aqueous solution, just in one step and at low or moderate temperatures. The remarkable activity has been associated to the presence of internal cavities where water molecules are occluded, leading to very reactive surface oxygen species. Besides, this catalyst is compared to another one, which is synthesized by a solvothermal method (ST). Although the as-prepared manganese oxide (ST) shows good catalytic activity, its performance is inferior to that displayed by the material obtained by a HT process

2. Experimental

2.1. Preparation method

Manganese oxide samples Mn-HT (hydrothermal) and Mn-ST (solvothermal) were prepared from 0.1 M manganese (II) acetate, $Mn(C_2H_3O_2)_2 \cdot 4H_2O$ (99%, Aldrich), solutions. The solvent was pure aqueous or ethylene glycol-water in 1:1 volume ratio, respectively. Ammonia was then added to adjust the pH value at 11 and the precipitation was facilitated. The suspensions were further introduced in autoclaves and treated at 180 ºC for 24 hours. The obtained precipitates were then filtered and dried in a stove at 100 ºC.

2.2. Catalyst characterization

Nitrogen adsorption measurements were performed on a Micromeritics ASAP 2010 physisorption analyzer at 77K. Brunauer–Emmett–Teller (BET) and Barret–Joyner–Halenda (BJH) methods were used for the surface area and pore size distribution determination using N_2 adsorption data. Samples were previously outgassed for at least 4 hours at 120 °C.

X-ray powder diffraction (XRD) patterns were registered at room temperature with a PAN analytical X'PERT POWDER diffractometer using Cu ($K\alpha$) radiation with λ=1.5418 Å. Fullprof program was used for Rietveld refinement and pattern matching analysis.

X-ray photoelectron spectroscopy (XPS) measurements were made on a Kratos Axis ultra DLD photoelectron spectrometer using a non-monochromatized Mg Kα X-ray source (hν = 1253.6 eV). Analyser pass energy of 50 eV was used for survey scans and 20 eV for detailed scans. Binding energies were referenced to the C1s peak from adventitious carbonaceous contamination, assumed to have a binding energy of 284.8 eV. XPS data were analysed using CasaXPS software. All the peaks of the corrected spectra were fitted with a Gaussian–Lorentzian shape function to peak fit the data.

Iterations were performed using the Marquardt method. Relative standard deviations were always lower than 1.5%.

Temperature programmed reduction (TPR) analyses were carried out in a Micromeritics Autochem 2920 instrument equipped with a thermal conductivity detector, operated under a 50 mL min^{-1} 10% H_2/Ar flow at temperatures between -50 and 800 °C, with a heating rate of 10 °C min^{-1}.

Spherical aberration corrected (C_s-corrected) Scanning Transmission Electron Microscopy (STEM) observation have been carried out in a Cold FEG JEOL Grand ARM 300, with double corrector, allowing a point resolution of 0.6 Å, equipped with the JEOL SDD EDS system (100mm2 x 2), a dual EELS Gatan 965 GIF Quantum ER; and in a FEI-Titan Low-Base microscope equipped with a C_s probe corrector, a monochromator and an ultra-bright X-FEG electron source. All measurements were performed at 300 kV. Prior observations, the samples were highly dispersed in ethanol for few minutes and few drops of the suspension formed were deposited onto holy carbon copper grids.

The SEM analyses were recorded in JEOL 7800 Prime. In order to acquire the best resolution and allow the observation of the surface of the crystallites, samples were not coated with either gold or carbon. Instead, we adopted gentle beam mode to decrease the chromatic aberration. Namely, the gun voltage applied was 5.5 keV, with a decelerating voltage -5 keV on the sample holder, giving a final landing energy of 0.5 keV on the samples. In order to avoid any misinterpretation, the samples observed in the SEM were the same ones as those observed in the TEM. Therefore, they were supported on carbon coated TEM Cu grids.

2.3. Catalytic tests

The catalytic activity was determined in a fixed bed micro-reactor with the reaction temperature controlled by employing a thermocouple placed in the catalyst bed. In most of the experiments the amount of toluene used was maintained in 200 vppm (0.02% molar) and the gas hourly space velocity was fixed in GHSV = 6,000 h^{-1}. In the standard experiments 99.98% of the feed consisted of synthetic gas (oxygen and helium in a 21/79 molar ratio) to give a $C_7H_8/O_2/He = 0.02/21.0/79.0$ molar ratio. In the experiments with water in the feed two amounts, 4 and 10 molar %, were used. Thus the feed was $C_7H_8/H_2O/O_2/He = 0.02/4.0/20.2/75.8$ or $0.02/10.0/18.9/71.1$ molar ratios. In the experiments with CO_2, 2 molar % of CO_2 was added to the feed maintaining the O_2/He ratio constant. Thus, the feed employed was $C_7H_8/CO_2/O_2/He = 0.02/2.0/20.6/77.4$ molar ratios whereas in the experiment with H_2O and CO_2 was $C_7H_8/H_2O/CO_2/O_2/He = 0.02/10.0/2.0/18.5/69.5$ molar ratios. Some experiments were undertaken with very high gas hourly space velocity GHSV = 240,000 h^{-1} maintaining the $C_7H_8/O_2/He = 0.02/21.0/79.0$ molar ratio. The reactants and reaction products were analyzed using an online gas chromatograph with TCD and FID detectors. Two chromatographic columns were used: (i) Porapak Q (for hydrocarbons and CO_2) and (ii) Molecular Sieve 5A (for oxygen and carbon monoxide). The reaction temperature was employed in the 100–350 ºC range. Conversion was calculated by two methods, through the differences between the inlet and outlet concentrations of toluene and by using the area of the reaction products (CO_2) and that of the reactant without reacting. These two procedures lead us to adjust the carbon balance with an accuracy of ±5%. Two analyses were done at each temperature after steady state was attained (ca. 30 min before the first analysis) and the results were averaged. A blank run was conducted in an empty reactor without catalyst until 350ºC, showing negligible (<1%) conversion.

3. Results and discussion

The catalytic performance has been studied by plotting the toluene conversion with the reaction temperature using low space velocities but in the industrial range. Figure 1 shows the evolution of the toluene conversion with the reaction temperature for the two manganese oxide catalysts synthesised. For our samples, 50 % conversion is achieved at 125 and 160 °C for Mn–HT and Mn-ST, respectively. Moreover, the 80 % conversion is achieved at 150 and 200 °C for Mn–HT and Mn-ST, respectively. It is noteworthy the low temperature, 175 °C, required for total toluene conversion using the most active catalyst, Mn-HT. In order to check the stability of the most active material, several catalytic cycles were conducted on Mn-HT. Figure 1 also shows the corresponding curves for six consecutive catalytic cycles and no appreciable differences were observed among the cycles, pointing out that this catalyst is highly stable.

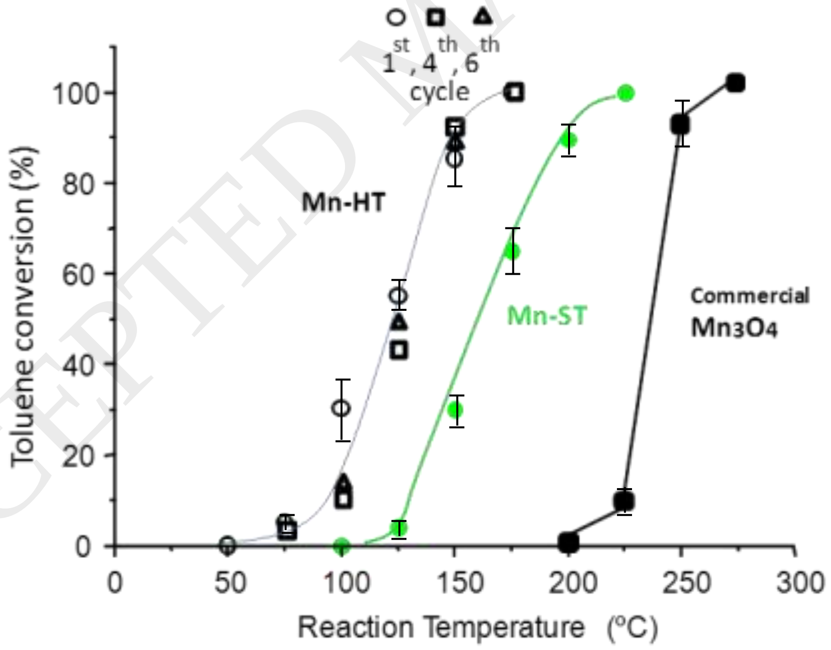

Figure 1. Variation of the toluene conversion with the reaction temperature for manganese oxide catalysts. 200 ppm in synthetic air. GHSV = 6000 h^{-1}.

Table 1 shows the comparison in terms of activity between our Mn-HT and Mn-ST materials and some catalysts reported in the literature, probing that the both catalysts prepared in this work, especially under hydrothermal conditions, have an outstanding good catalytic performance in the catalytic oxidation of toluene.

Table1. Comparison of the catalyst activity between this work and literature.

Catalyst	T_{50} (ºC)	T_{80} (ºC)	Toluene concentration (ppm)	GHSV (h^{-1})	Ref.
Mn-HT	125	150	200	6000	This work
Mn-ST	165	200	200	6000	This work
Mn-HT	250	260	200	240000	This work
Mn-ST	265	280	200	240000	This work
Mn_2O_3	256	--	1000	--	[18]
Mn_3O_4	220	230	1000	19100	[38]
Mn_3O_4	230	240	1000	180000	[39]
Mn_3O_4	240	248	2000	15000[a]	[14]
Mn_2O_3	275	280	2000	15000[a]	[14]
MnO_2	345	353	2000	15000[a]	[14]

[a] in ml h^{-1} $g^{-1}_{catalyst}$

Manganese oxide hydrothermally prepared (Mn-HT) can totally remove toluene using low space velocities at very low temperature (175ºC). This behaviour is stable and after 6 cycles similar light-off curve is observed. This stable performance is likely due to the fact that the temperature this material has been previously heat-treated (180ºC) is higher than that required for total conversion (175ºC) and then the structural and surface modifications after the catalytic tests are not important. However, using high space velocities the temperatures required for total conversion already exceed 180ºC and then a drop in the reactivity is observed. This drop has been demonstrated undertaking an experiment at low space velocity with catalyst previously used at high space velocity. Then it is observed an important activity fall. For example, using low space velocity 50% conversion is obtained at 125ºC with the fresh or catalysts used until 175ºC; however, 50% conversion is obtained at ca. 175ºC with the catalyst previously used at high space velocity (this experiment required ca. 275ºC for total conversion).

As Mn-HT is the most active catalyst, different reaction conditions were studied. In the industrial effluents, VOCs are usually emitted in streams containing other components, mainly water and carbon dioxide. Accordingly, the performance of Mn-HT catalyst was evaluated at 125 ºC in the presence of different concentrations of these compounds (Figure 2). In the case of the addition of water to the feed, increasing amounts of H_2O % up to 10 mol% were used. Interestingly, decreasing activity is not observed in any case. Even at low H_2O concentrations a slight positive effect is attained. Additionally, a complete cycle was also run using 4 wt.% water in the feed (curve not shown). Interestingly, total conversion is observed at only 150ºC which is lower than that temperature at which total conversion is achieved in the absence of water (175ºC) (see Figure 1).

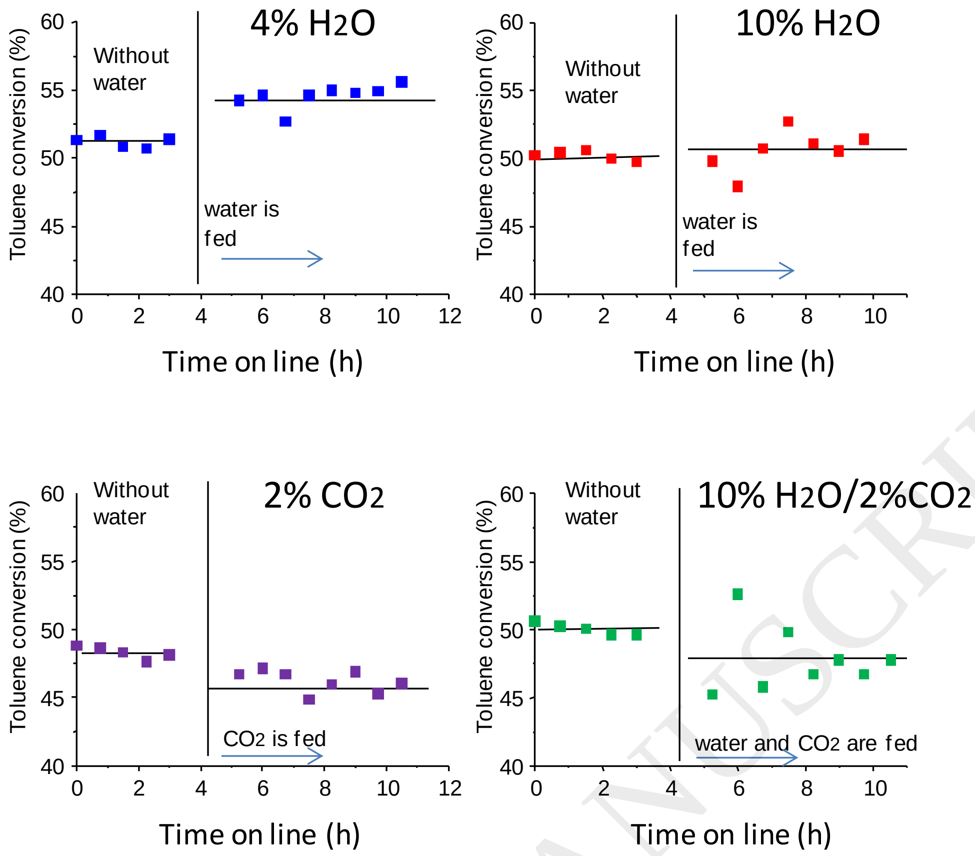

Figure 2. Toluene conversion under different reaction feeds. Toluene concentration: 200 ppm. Reaction temperature: 125 °C. GHSV: 6000 h^{-1}.

Moreover, the addition of CO_2 to the feed was not deleterious as only a subtle decrease of conversion is observed. The simultaneous addition of water and carbon dioxide did neither have an influence on the catalytic performance. Therefore, Mn-HT shows an outstanding activity and stability in relevant conditions.

In order to explain the remarkable catalytic activity of these catalysts a detailed characterization has been conducted. Firstly, textural characteristics of the samples were analysed by N_2 adsorption/desorption isotherm measurements. Data are shown in Figure 3. Unexpectedly, Mn-HT displays a remarkably lower S_{BET} value than Mn-ST, 29 vs. 108 m^2 g^{-1}, ruling out the relevant role of this parameter on the catalyst performance. The isotherms recorded for these materials correspond to Type IV isotherms usual for mesoporous samples. In all isotherms the hysteresis loop is rather narrow, making the denomination of the hysteresis type not easy. We use the adsorption branch of the isotherm to determine the mesopore size distribution, eluding the nitrogen adsorption artefact due to the steep desorption at P/P_0 of 0.4-0.5. It is noteworthy that the mesopore volume for the sample obtained under solvothermal conditions (Mn-ST) shows a remarkable contribution of the pores lower than 10 nm, whereas this contribution is marginal for the Mn oxide prepared under hydrothermal conditions.

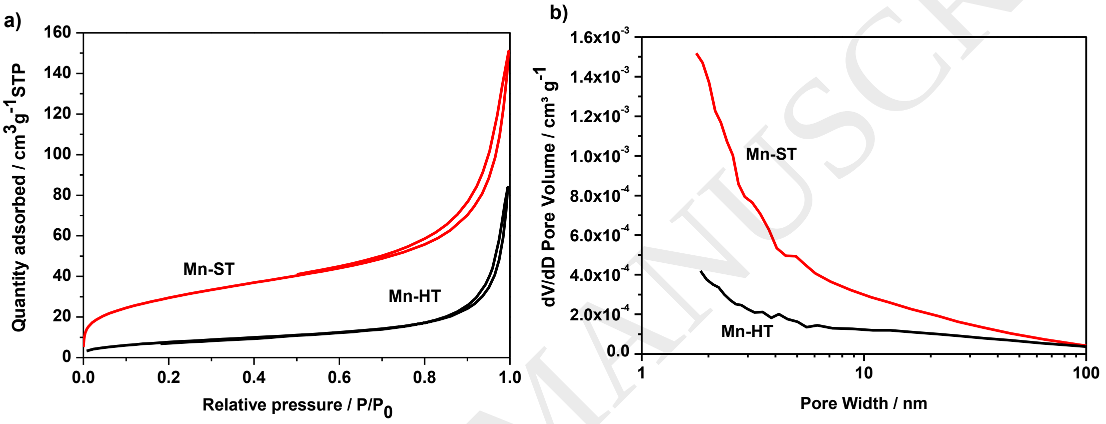

Figure 3. a) N_2 adsorption/desorption isotherms and b) pore-size distributions for manganese catalysts.

Therefore, the synthesis under solvothermal conditions favours the formation of intraparticle porosity, which is hardly created under hydrothermal conditions, as corroborated later by microscopy analyses.

The main crystalline phase observed in both samples is Mn_3O_4 which is reported to be the most active crystalline phase of the manganese oxides for total oxidation reactions [14,38]. XRD patterns (Figure 4) permit to identify unambiguously that the two manganese catalysts present the spinel (AB_2O_4, hausmannite) type structure belonging to the tetragonal crystal system and $I4_1/amd$ space group. The unit cell comprises 32 oxide ions and there are 8 Mn^{2+} ions occupying the tetrahedral (A) sites and 16 Mn^{3+} ions located in the octahedral (B) ones.

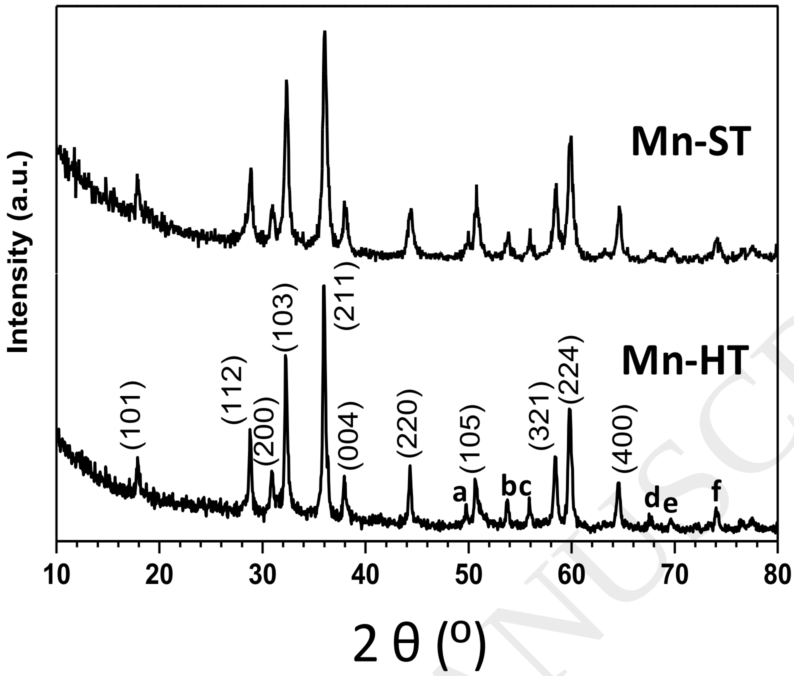

Figure 4. XRD patterns of manganese oxide catalysts. In both cases the only phase detected is Mn_3O_4. The small diffractions a, b, c, d, e and f correspond to (204), (312), (303), (402), (305) and (413), respectively.

Average crystallite sizes calculated from XRD patterns applying Double-Voigt approach reveals that the solvothermal synthesis produces materials with smaller crystallite size than the hydrothermal one, 9 and 19 nm respectively, which is also in line with the highest surface area of the Mn-ST sample. The higher particle size under hydrothermal conditions can be due to the fact that ethylene glycol is a less polar solvent than water, thus the solvation energy of the oxide/hydroxide phase is lower than in pure water. This leads to a higher initial energy of the oxide/hydroxide before nucleation and a lower energy barrier has to be overcome for crystallization. Consequently, the nucleation rate is higher in solvent-rich solutions, preventing the growth of bigger crystallites.

Moreover, structural analyses were made applying Rietveld analyses for both materials. The excellent results of refinement (Table 2) indicate the great influence of the solvent used during the synthesis procedure on the tetragonal cell parameters, a contraction of the unit cell occurs in “a” direction and elongation in the direction of “c” axis take place by increasing the mean particle size <d>. Both samples show a defect in its structure. In fact, in the catalysts studied both cationic and anionic vacancies have been detected in the spinel structure. The refinements were done assuming that the octahedral sites are fully occupied by Mn^{3+} cations. SOF (site occupation factors) values for Mn^{2+} and oxygen atoms (Table 2) point out a defect in the cationic and anionic sites, respectively, which could explain the relevant activity of both catalysts. For the Mn-ST sample, 10% deficiency approximately exists in cationic sites containing Mn^{2+} that can arise from partial oxidation of Mn^{2+} to Mn^{3+} leading to formation of cationic vacancies. These are mainly compensated by the deficiency in the anionic sites (~8%) through formation of anionic vacancies and in fewer amounts via presence of interstitials (e.g., OH^{-}). The calculated density for such sample from refinement data reveals a defect spinel structure, with a value of 4.63 g cm^{-3} in contrast with 4.86 g cm^{-3} for the ideal spinel structure (bulk material).

Table 2. Rietveld analyses.

Sample	Mn-ST	Mn-HT
Phase name	Mn_3O_4	Mn_3O_4
Space group (No.)	I 41/a m d (141)	I 41/a m d (141)
R_{Bragg}	0.315	0.234

a = b (Å)	5.765	5.763
c (Å)	9.425	9.444
$c/\sqrt{2}\,a$	1.14	1.16
ρ (g/cm^3)	4.630	4.737
V (Å^3)	313.31	313.75
R_{exp}	0.85	0.92
R_p	0.80	0.88
R_{wp}	1.01	1.12
*GOF	1.18	1.21
**s.o.f. / Mn^{2+}	0.89	0.93
**s.o.f. / Mn^{3+}	1.00	1.00
**s.o.f. / O^{2-}	0.92	0.97

*GOF: goodness of fit. It compares R_{wp} with R_{exp}. GOF=1 means the model is as good as possible. GOF values less than 4 are acceptable.
**s.o.f.: site occupancy factor. s.o.f.=1 means every equivalent position for xyz is occupied by that atom and s.o.f.<1 means some of the sites are vacant.

On the other hand, Mn-HT sample showed a less defective spinel structure with a calculated density of 4.74 g cm^{-3}, in line with its higher mean crystallite size. However, a higher activity is observed for this catalyst. Significantly, 7% deficiency approximately exists in cationic sites containing Mn^{2+} but, contrary to what happened for the Mn-ST catalyst, defects are not mainly compensated by the deficiency in the anionic sites (~2%) through formation of anionic vacancies but mainly by the presence of higher amounts of interstitials, likely structural water or interstitial OH^{-}. Therefore, the insertion into the crystalline structure of these species during the hydrothermal synthesis could be the driving factor for the better catalytic performance of this material. This fact could also explain the higher activity found in presence of water since the possible loss of structural water at those temperatures needed to reach full toluene conversion could be reduced under humid conditions.

The mixed oxidation state of Mn, typical of hausmannite spinel, was also confirmed by the XPS results (Figure 5a) were the Mn 3s splitting value of 5.7 eV corresponds to the mixed valence state of Mn^{2+} and Mn^{3+} with characteristic splitting values of 5.9 eV and 5.5 eV, respectively [40, 41]. The Mn $2p_{3/2}$ peak (Figure 5b) is centered at 641.3 eV and the Mn $2p_{1/2}$ peak at 653.1 eV, with a splitting of 11.8 eV, which is in good agreement with literature values [40, 41]. Moreover, deconvolution of Mn 2p spectral region allowed calculating a Mn^{2+}: Mn^{3+} ratio 1:1.8 which is in good agreement with the stoichiometric value (1:2) but showing no differences among Mn-HT and Mn-ST catalysts. The slight discrepancies between the Mn^{2+}: Mn^{3+} ratio determined by XPS and the bulk can be related to the presence of oxygen/cationic vacancies in the surface.

The asymmetrical O 1s signal can be deconvoluted into two components (Figure 5c). The peak at 529.5 eV is attributed to the surface lattice oxygen O^{2-} whereas the broad shoulder at a higher BE (531.3 eV) assignment is more difficult, as this feature could either be the result of hydroxyl groups or alternatively might be due to the presence of oxygen vacancies, surface adsorbed oxygen, or carbonate species.

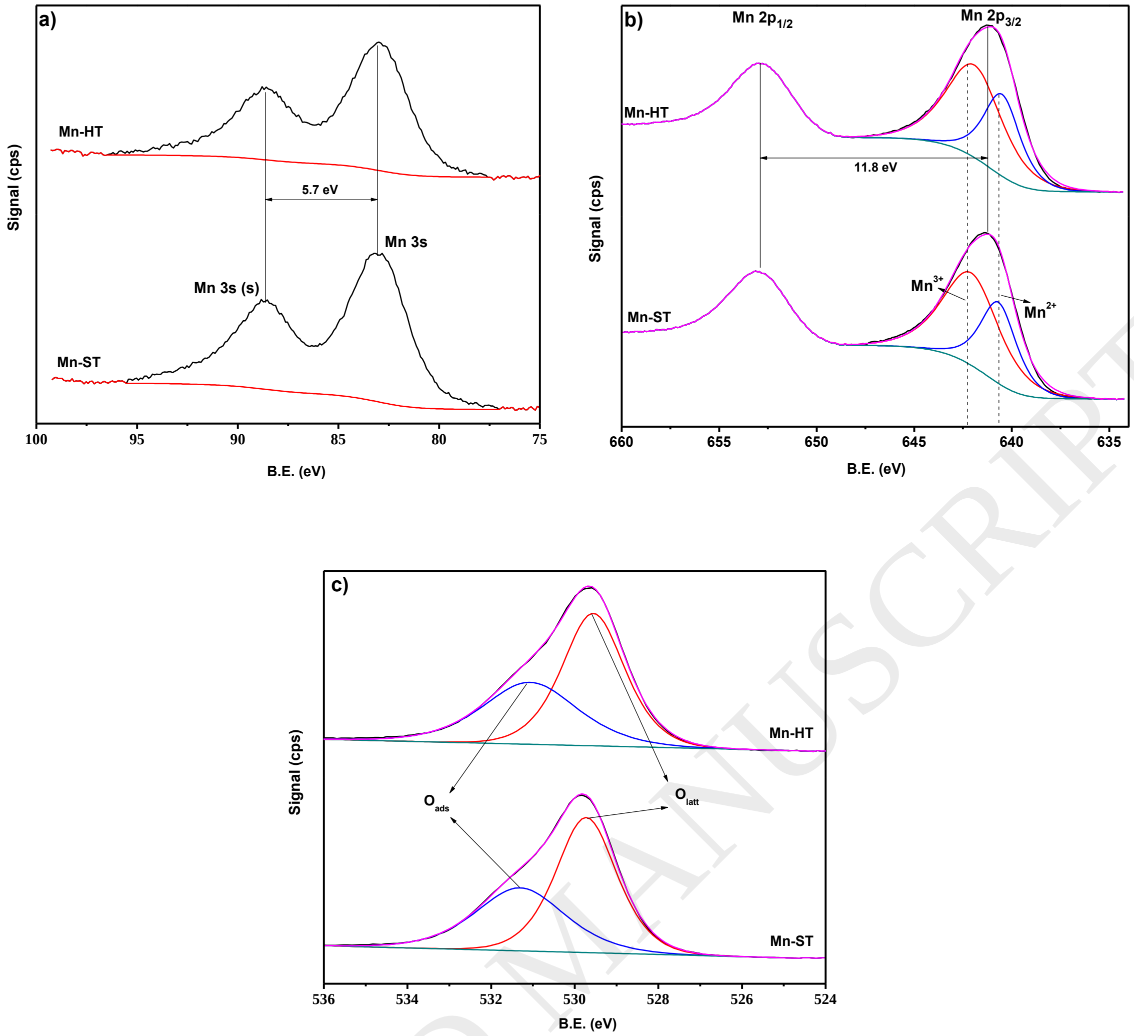

Figure 5. XPS spectra of the (a) Mn 3s region, (b) Mn 2p region and (c) O 1s region of the manganese oxide catalysts.

The reactivity of the oxygen species was investigated by H_2-TPR analysis. The TPR profile of the Mn_3O_4 samples (Figure 6) shows a low-temperature band around 200-300ºC, which can be attributed to the reduction of Mn^{3+} ions located in the tetrahedral sites of the hausmannite lattice, and a wide signal in the 300–500ºC temperature range, due to the hausmannite reduction ($Mn_3O_4 \rightarrow MnO$). Since MnO is the final reduction product (terminating at ca. 700 ºC), the two peaks should reveal the reduction of two different Mn^{3+}-O bonds (to MnO) that are available in Mn_3O_4 [38]. The H_2 consumption (4.3 mmol g^{-1}), related to the $Mn_3O_4 \rightarrow MnO$ step, is in close agreement with the theoretical data. Although both Mn-catalysts present a similar profile, some relevant differences can be clearly observed in the low temperature reduction band. In this temperature range, it is clearly seen that Mn^{3+} in the tetrahedral sites of the hausmannite lattice are in two different chemical environments, being these species reduced around 200 ºC and 250 ºC, respectively. In line with Rietveld refined data, these two different sites could be tentatively related to the presence of cationic vacancies compensated by either interstitials or anionic vacancies, respectively, being the reducibility of the former higher than that observed for the latter. Therefore, it can be observed in Figure 6 that there is a higher proportion of highly reactive oxygen species associated to cationic vacancies compensated by interstitials in the Mn-HT sample, which is also in line with its higher activity.

In the present article it has been observed that the maximum of the main reduction bands of manganese oxides in the TPR experiments arise at ca. 350ºC whereas toluene can be converted on manganese oxide catalysts at reaction temperatures lower than 200ºC. However, if we see in detail the TPR profiles, we can notice that the onset temperatures of the first reduction bands are observed at temperatures below 140ºC. In any case, the conditions used in the TPR experiments are very different to those of our toluene oxidation reaction and then the reduction of the catalyst in both environments can be very different.

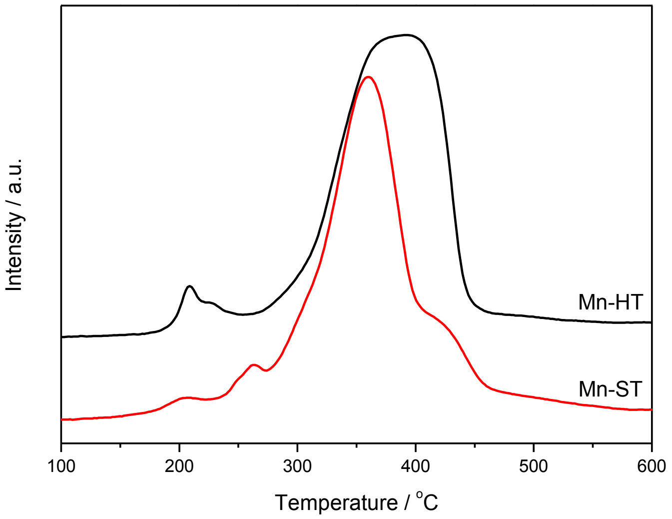

Figure 6. H_2-TPR for the manganese oxide catalysts.

Electron microscopy observations show that the material named as Mn-ST exhibits a predominant phase composed of nanoparticles of around 10-40 nm (Figures 7a, 7b and S1). In all cases, the particles exhibited very good crystallinity in good agreement with the XRD data obtained and they can be indexed assuming $I4_1/amd$ symmetry and lattice constants similar to the bulk Mn_3O_4, a ≈ 5.7 Å and c ≈ 9.4 Å. Figure 7b corresponds to a representative nanoparticle observed along the [111] orientation; a closer look at the atomic distribution is shown in Figure 7c with the model superimposed which allows the identification of all atoms in the structure. In this model, Mn is represented in green while O appears in red. Considering that all data was recorded using a High Angle Annular Dark Field Detector (HAADF) the contrast observed is dependent on the atomic number and thickness of the material. Therefore, the contrast variations observed in the nanoparticles analyzed (Figure 7a) are owed to the presence of cavities/roughness at the surface of the material, which is in line with the presence of pores lower than 5 nm, as observed by N_2 adsorption data.

The material obtained by hydrothermal synthesis, Mn-HT, presents a similar shape and a slightly higher particle size than the Mn-ST sample. Figure 7d depicts a low magnification image confirming the similar morphology of the material obtained under hydrothermal conditions composed of nanoparticles with various sizes. The crystallinity for every particle observed was also found to be very good as was the case for Mn-ST, see Figure 7e, in perfect agreement with the tetragonal symmetry $I4_1/amd$. The high-resolution data, Figure 7e and 7f, allow the visualization of the atomic distribution of the atoms along the [011] orientation, where the Mn atoms appear as green spheres while O are in red. Surprisingly, cavities/roughness are again apparent, even in a higher amount (see Fig. S1d-S1f), despite the fact that the presence of surface mesopores is hardly observed by N_2 adsorption data. Therefore, the internal cavities/vesicles instead of surface mesopores are predominantly created during the hydrothermal synthesis, where water molecules could be occluded leading to highly active oxygen surface species, according to TPR data.

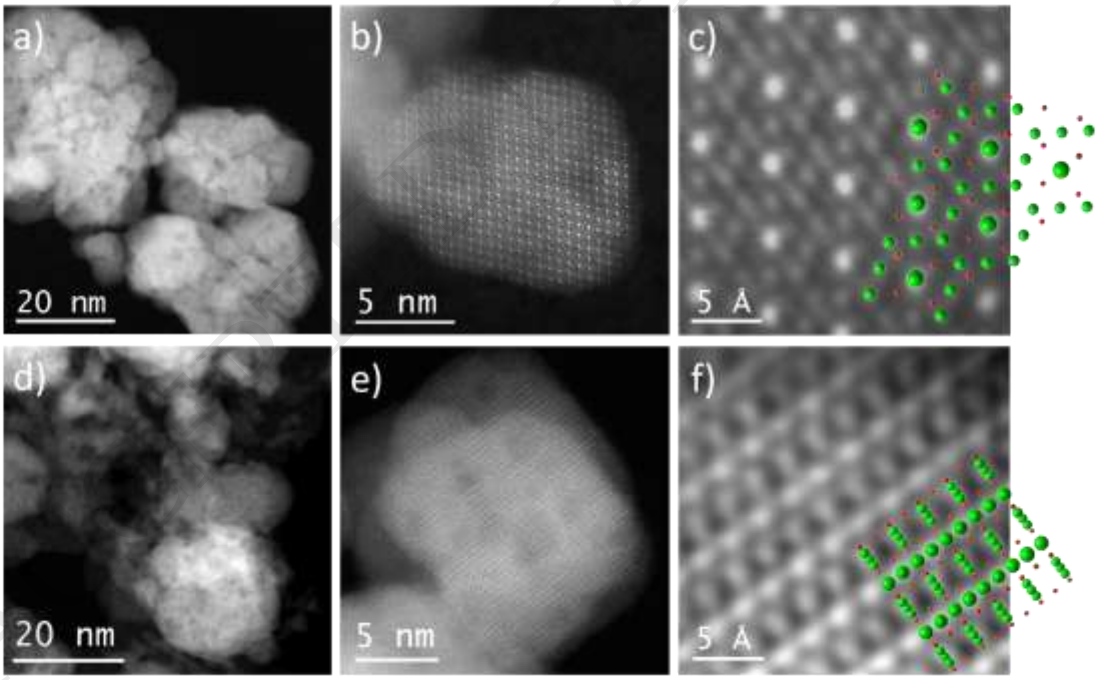

Figure 7. C_s-corrected STEM-HAADF data. a) Low-magnification image showing several Mn-ST nanoparticles. b) High-resolution image of a Mn-ST isolated nanoparticle along the [111] zone axis. c) A closer look of the structure of the Mn-ST nanoparticle with the model superimposed. d) Low-magnification image of Mn-HT material. e) An isolated Mn_3O_4-HT nanoparticle along the [011]

orientation. f) Enlarged image of the particle shown in e) with the model superimposed. Green spheres correspond to the Mn while O atoms appear as red spheres.

The chemical composition for both samples was corroborated by means of Energy dispersive X-ray Spectroscopy (EDS) and Electron Energy Loss Spectroscopy (EELS), see Figure 8**,** concluding that the Mn and O are equally distributed with no detectable compositional variations in any case. Figure 8a corresponds to the EDS map recorded over several nanoparticles proving the homogeneous composition for every particle. The EELS spectrum image appears in Figure 8b. For this case, an isolated nanoparticle was analyzed in order to observe any variations along the nanoparticle (if any). A homogeneous distribution was obtained for both samples.

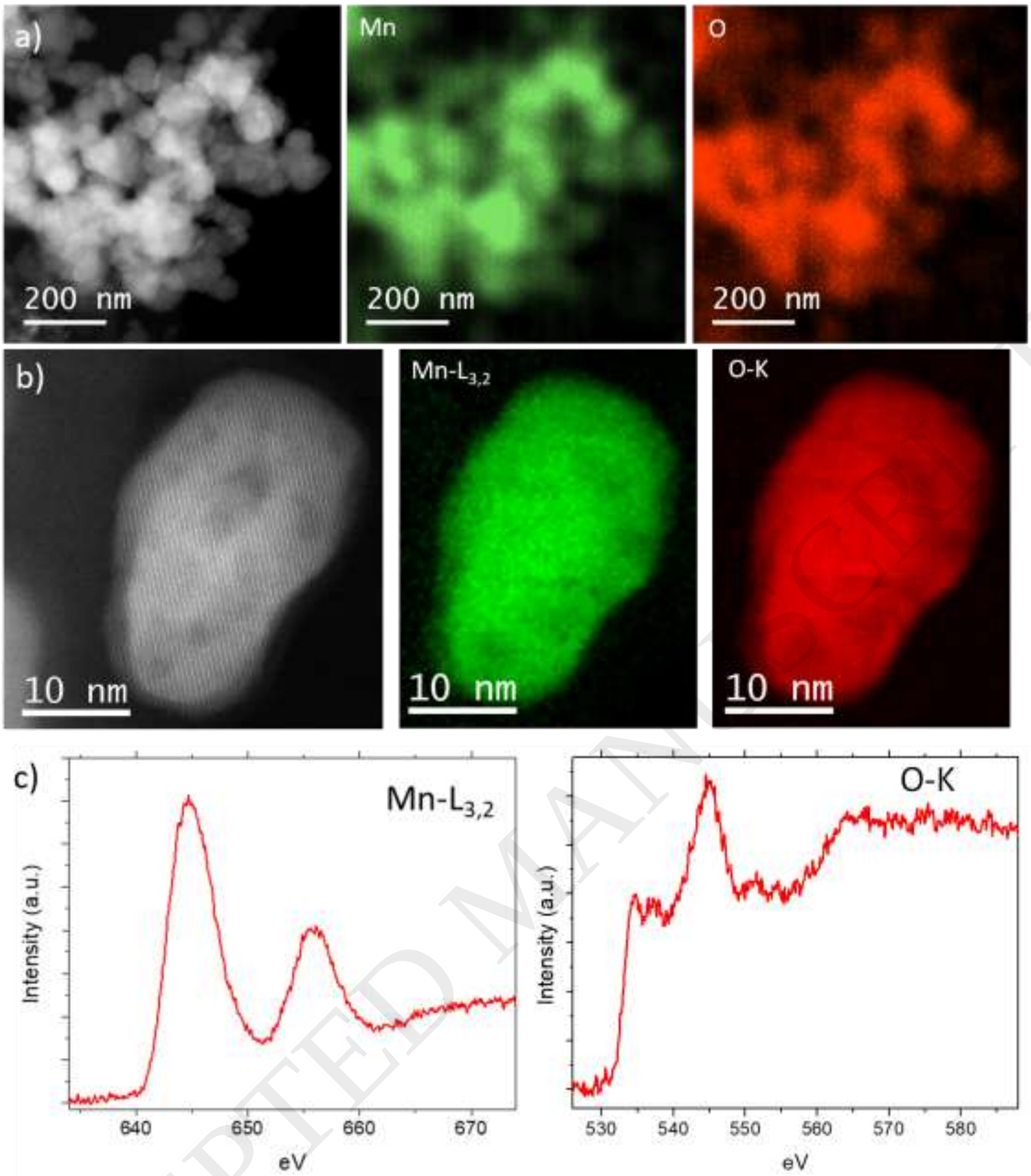

Figure 8. Study by TEM of Mn-HT catalyst. a) EDS mapping analysis of several nanoparticles which confirms the presence of Mn (green map) and O (red map). b) EEL spectrum image of a Mn-HT nanoparticle showing the perfect concordance between the Mn and O. c) EEL spectra of the signals extracted corresponding to Mn and O edges respectively.

Considering the similarities between the products obtained by means of both synthetic methods, we believe that the differences observed in their catalytic performance can be explained in terms of the type of cavities created during the preparation method. As already mentioned, all NPs show contrast variations in the images that are attributed to the presence of a rough surface, as the chemical composition has been found to be homogeneous with the same Mn:O ratio. With the intention of gaining more information about this assumption SEM analyses were performed (Figure 9) showing that for Mn-ST there are more interparticle voids, resulting in a higher surface area. For both samples, Mn-ST and Mn-HT, the morphology of the materials is very similar observing three main products sphere-like particles, elongated particles with plate morphology and nano-fibers type formations, which could be attributed to manganese hydrated phases [42], see Figure 9. Figures 9a and 9b present the SEM observations at low and at high magnification for the Mn-ST material. It is possible to observe the presence of spherical-like particles all over the sample. In the high-resolution SEM data it is possible to visualize the channels opened to the surface of these nanoparticles, which make them look like if they were agglomerated entities but from the STEM analysis it can be inferred that they are single individual crystals.

After observation of the Mn-HT at low-magnification Figure 9c, it is apparent a more heterogeneous material, with the plates and nano-fibers also present. These structures were also observed in Mn-ST but into a less extent. By looking closer at the nanoparticles formed by this synthetic method, Figure 9d, it is also possible to visualize a similar morphology as observed for Mn-ST, but in this case less porosity appears, making the material more compact exposing less open pores opened to the surface giving as a result a lower adsorption capability.

Meanwhile, despite the similarities, for Mn-HT the particles are more compact and exposing less accessible pores opened to the surface. By analysing several nanoparticles and in line with XRD, H_2-TPR and N_2 adsorption data, the Mn-HT contains more internal cavities where water molecules can be retained, leading to highly active surface oxygen vacancies. These sites could act as reaction sites increasing the catalytic performance.

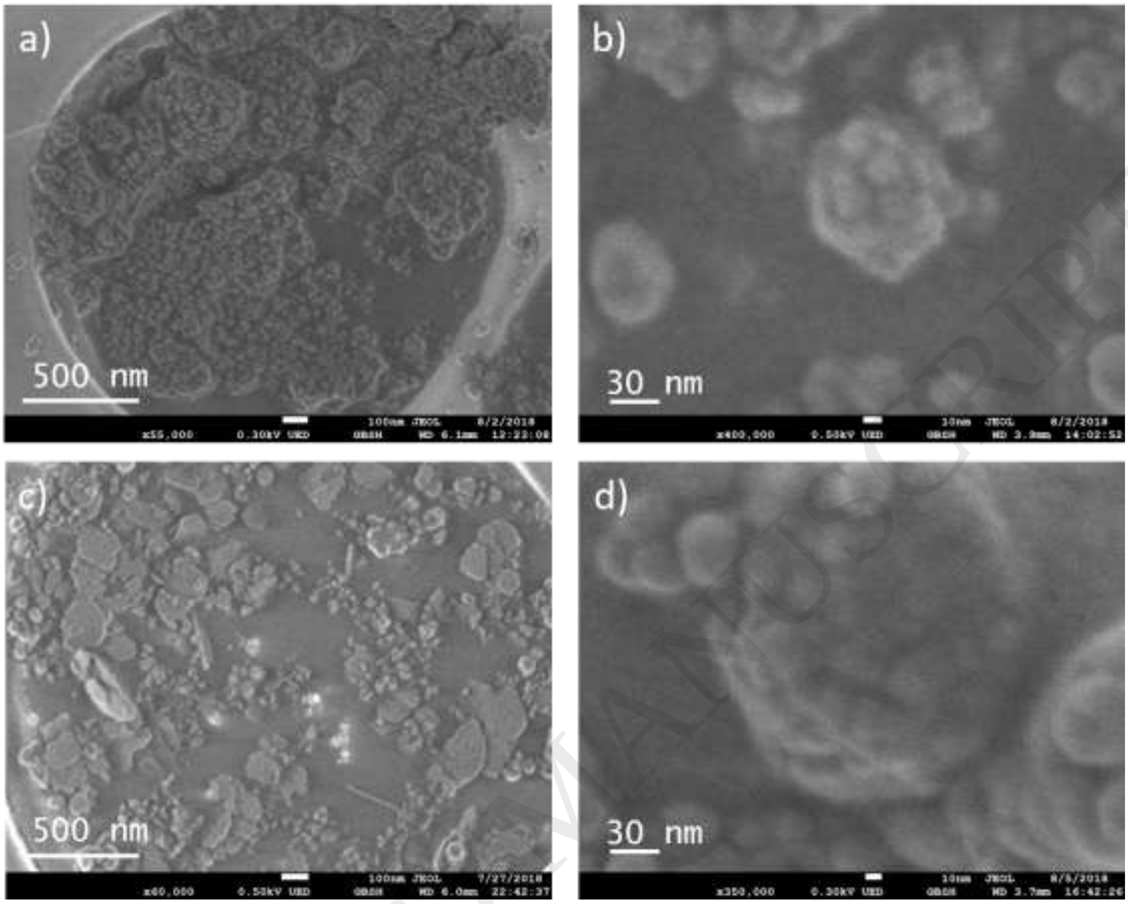

Figure 9. SEM observations of Mn-ST, a) Low-magnification and b) High-magnification images. And Mn-HT c) Low-magnification and d) High-magnification images.

Manganese oxide synthesized by an easy hydrothermal method show very high catalytic activity and using low space velocities can completely remove toluene at very low temperatures (150-175ºC). This performance does not vary and after several cycles the same behaviour is observed. This stable behaviour is likely due to the fact that the temperature this material has been heat-treated (180ºC) is higher than that required for total conversion and then the structural and surface modifications after the catalytic tests are not important. According to the high catalytic stability observed, the characteristics of the used catalyst have changed little compared to the fresh catalyst. Deconvoluted XPS spectra of the used Mn-HT catalyst (Figure S2) shows a slight shift of ca. 0.2 eV to higher binding energies in the Mn2p region probably due to a slight oxidation of Mn^{3+} species to Mn^{4+}. Moreover, the Mn^{2+} : Mn^{3+} ratio increases from 1:1.80 to 1:1.85 attributed to a slightly lower presence of oxygen/cationic vacancies in the surface. This fact is also confirmed by the deconvolution in the O1s region which shows a value of 1.6 for the Olatt/Oads ratio compared with 1.4 value in the fresh catalyst. In the XRD patterns (Figure S3) the same crystalline phase has been observed (Mn_3O_4) with just a slight decrease in the width of the peaks and consequently a slight increase in the mean crystallite size after use. It has been also observed a small fall in the surface area for the spent catalyst (from 29 to 25 m^2/g). The electron microscopy observations prove the good crystallinity of the reacted material, same of the as-synthesized one, and also the chemical analysis performed by means of EEL spectral imaging shows a homogeneous distribution of Mn and O after reaction (Figure S4). From electron microscopy perspective, it is difficult to assure that any significant transformation took place after use, as both materials were very similar in terms of composition, particle size and structure. Nevertheless, we cannot discard the possibility of a slight increment of the initial good crystallinity in accordance with the XRD observations, as a result, possibly, of the thermal treatments that the catalyst underwent. It is important to keep in mind that electron microscopy is a more local technique while XRD gives a more averaged information of the materials (Figure S5).

Interestingly, the hydrothermally prepared catalyst presents a catalytic activity higher than that synthesized by a solvothermal method which presents much higher surface area and lower crystallite size. The extremely high catalytic activity of the Mn_3O_4 catalyst prepared by the hydrothermal method can be due to the presence of oxygen surface species which are highly reactive. The presence of Mn_3O_4 nanoparticles with a high concentration of Mn^{3+} at the tetragonal distorted cationic sites does likely play an important role. Interestingly, there are internal cavities/vesicles in the Mn_3O_4 structure which induces the presence of structural water.

4. Conclusions

Highly active manganese oxide catalyst has been synthesised using a simple and green synthesis method employing a hydrothermal procedure. A catalyst with remarkably higher activity is obtained by this method in spite of the fact that the surface area of the hydrothermal catalyst is ca. 4 times lower than that of the catalyst prepared by a solvothermal method. This catalyst has been tested in the total oxidation of toluene showing total conversion at only 175ºC in the absence of water and, more remarkably, at 150ºC using low concentrations of water (4 mol%). This performance hardly varies and after 6 catalytic cycles similar results are observed. In view of the characterization of these catalysts and in line with literature data, the outstanding catalytic activity of the Mn_3O_4 catalyst prepared by the hydrothermal method can be ascribed to the presence of highly reactive oxygen surface species. This species are likely promoted due to the existence of Mn_3O_4 nanoparticles with a relevant amount of Mn^{3+} at the tetragonal distorted cationic sites, likely compensated by structural water at the anionic sites. Interestingly, the presence of structural water seems to be a consequence of the formation of internal cavities/vesicles in the Mn_3O_4 crystalline structure.

Acknowledgements

AM and YZ acknowledge The Centre for High-resolution Electron Microscopy (CħEM), supported by SPST of ShanghaiTech University under contract No.

EM02161943. Electron microscopy analyses were performed at Centre for High-Resolution Electron Microscopy (*CħEM*), ShanghaiTech University. AM acknowledges the National Natural Science Foundation of China through the projects NSFC NFSC-21850410448 and NSFC- 21835002. Authors from UCM thank Santander-UCM institution (PR41/17-20951 project) and MINECO (MAT2017-84118-C2-2-R project) and UCM CAI centers (XRD and EM). TG and JML thank Regional Aragon Government (DGA) under the research groups support programme. Some of the STEM analyses were conducted at the Laboratorio de Microscopias Avanzadas, Universidad de Zaragoza, Spain. R. A. acknowledges support from Spanish MINECO grant MAT2016-79776-P (AEI/FEDER, UE). Authors from UV thank MINECO (MAT2017-84118-C2-1-R project) for funding.

References

1 L. F. Liotta, Appl. Catal. B: Environ. 100(3-4) (2010) 403–412.

2 Z. Chen, J. Ma, R. Zhou, Appl. Surf. Sci. 465 (2019) 15–22.

3 R. Balzer, L. F. D. Probst, V. Drago, W. H. Schreiner and H. V. Fajardo, Braz. J. Chem. Eng. 31 (2014) 757-769.

4 B. Solsona, T.E. Davies, T. García, I. Vázquez, A. Dejoz and S.H. Taylor, Appl. Catal. B: Environ. 84 (2008) 176–184.

5 T. García, D. Sellick, F. Varela, I. Vázquez, A. Dejoz, S. Agouram, S. H. Taylor, and B. Solsona, Appl. Catal. A: Gen. 450 (2013) 169–177.

6 M. Popova, A. Ristic, M. Mazaj, D. Maučec, M. Dimitrov and N. Novak Tušar. ChemCatChem. 6 (2014) 271–277.

7 M. Popova, Á. Szegedi, Z. Cherkezova-Zheleva, A. Dimitrova and I. Mitov. Appl. Catal. A: Gen. 381 (2010) 26–35.

8 S. Boycheva, D. Zgureva, M. Václavíková, Y. Kalvachev, H. Lazarova and M. Popova. J. Hazardous Materials, 361 (2019) 374-382.

9 J. Luo, Q. Zhang, A. Huang and S. L. Suib, Micropor. Mesopor. Mater. 35-36 (2000) 209–217.

10 C. Lahousse, A. Bernier, P. Grange, B. Delmon, P. Papaefthimiou, T. Ioannides and X. Verykios, J. Catal. 178 (1998) 214–225.

11 W. Si, Y. Wang, Y. Peng, X. Li, K. Lim, J. Li, Chem. Commun. 51 (2015) 14977-14979.

12 S. S. T. Bastos, J. J. M. Orfao, M. M. A. Freitas, M. F. R. Pereira and J. L. Figueiredo, Appl. Catal. B: Environ. 93 (2009) 30–37.

13 S. S. T. Bastos, S. A. C. Carabineiro, J. J. M. Órfao, M. F. R. Pereira, J. J. Delgado and J. L. Figueiredo, Catal. Today, 180 (2012) 148–154.

14 S. C. Kim and W. G. Shim, Appl. Catal. B: Environ., 98 (2010) 180–185.

15 H.Pan, Y. Jian, C. Chen, C. He, Z. Hao, Z. Shen, H. Liu, Environ. Sci. Technol. 51 (2017) 6288-6297.

16 H. Sun, S. Chen, P. Wang and X. Quan, Chem. Eng. J., 178 (2011) 191–196.

17 Y. S. Ding, X. Shen, S. Sithambaram, S. Gomez, R. Kumar, M. B. Vincent and S. L. Suib, Chem. Mater. 17 (2005) 5382–5389.

18 Z. Sihaib, F. Puleo, J. M. Garcia-Vargas, L. Retailleau, C. Descorme, L. F. Liotta, J. L. Valverde, S. Gil and A. Giroir-Fendler, Appl. Catal. B: Environ. 209 (2017) 689-700.

19 J. Chen, X. Chen, W. Xu, Z. Xu, J. Chen, H. Jia, J. Chen, Chem. Eng. J. 330 (2017) 281-293.

20 Y. Wang, L. Zhang, L. Guo, ACS Appl. Nano Mater. 1 (2018) 1066−1075.

21 J. A. Darr, J. Zhang, N. M. Makwana, X. Weng, Chem. Rev. 117 (2017) 11125−11238.

22 M. Shandilya, R. Rai & J. Singh, Advances in Applied Ceramics, 2016, DOI: 10.1080/17436753.2016.1157131.

23 B. Patel, M. Guo, A. Izadpanah, N. Shah, K. Hellgardt, Bioresource Technology 199 (2016) 288–299.

24 G. Canua, V. Buscaglia, Cryst. Eng. Comm. 19 (2017) 3867-3891.

25 Q. Yang, Z. Lu, J. Liu, X. Lei, Z. Chang, L. Luo, X. Sun, Progress in Natural Science: Materials International, 23, 4, (2013) 351-366.

26 X. Li, X. Lv, N. Li, J. Wu, Y.-Z. Zheng, X. Tao, Appl. Catal. B: Environ. 243 (2019) 76-85.

27 B. Naresh, D. Punnoose, S. Srinivasa Rao, A. Subramanian, B. Raja Ramesh, Hee-Je Kim, New J. Chem. 42 (2018) 2733-2742.

28 B.Jansi Rani, G.Ravi, R. Yuvakkumar, S. Ravichandran, Fuad Ameen, S. Al Nadhary, Renewable Energy 133 (2019) 566-574.

29 T. Tsoncheva, G. Issa, I. Genova, M. Dimitrov, D. Kovacheva, J. Henych, M. Kormunda, N. Scotti, J.Tolasz, V. Štengl, Microp. Mesop. Mater. 276 (2019) 223-231.

30 H.-R. Xia, W.-T. Sun, L.-M Peng, Chem. Commun. 51 (2015) 13787-13790.

31 X. Jia, X. Wu, B. Liu, Dalton Trans. 47 (2018) 15506-15511.

32 G. Qiu, H. Huang, S. Dharmarathna, E. Benbow, L. Stafford, S.L. Suib, Chem. Mater. 23(17) (2011) 3892–3901.

33 H-J Chen, W. Tian, W. Ding, Adsorption Science & Technology, 36 (2018) 1100-1111.

34 M. P. Pico, I. Álvarez-Serrano, M. L. López, M. L. Veiga, Dalton Trans., 43 (2014) 14787.

35 S. Ge, X. Shi, K. Sun, C. Li, J. R. Baker, M. M. Banaszak Holl, B. G. Orr, J. Phys. Chem. C 113 (2009) 13593–13599.

36 C. Doornkamp, V. Ponecr, J. Molec. Catal. A: Chem. 162 (2000) 19–32.

37 S. Todorova, A. Naydenov, H. Kolev, G. Ivanov, A. Ganguly, S. Mondal, S. Saha, A. K. Ganguli, Reac. Kinet. Mech. Cat. 123 (2018) 585–605.

38 M. Piumetti, D. Fino and N. Russo, Appl. Catal. B: Environ., 163 (2015) 277-287.

39 J. Li, L. Li, F. Wu, L. Zhang and X. Liu, Catal. Comm. 31 (2013) 52–56.

40 J. W. Lee, A. S. Hall, J. D. Kim and T. E. Mallouk, Chem. Mater. 24 (2012) 1158–1164.

41 G. Zhao, J. Li, W. Zhu, X. Ma, Y. Guo, Z. Liu and Y. Yang, New J. Chem.40 (2016) 10108-10115.

42 Y. Ruiz-Heredia, I. Álvarez-Serrano, M.L. López, C. Pico and M.L. Veiga, J. Supercrit. Fluids, 78 (2013) 21-27.